Experimental and numerical investigation of the mechanical behavior of the AA5383 alloy at high temperatures

Rou Du, Charles Mareau, Yessine Ayed, Eliane Giraud, Philippe Dal Santo

Experimental and numerical investigation of the mechanical behavior of the AA5383 alloy at high temperatures

Rou Du*, Charles Mareau, Yessine Ayed, Eliane Giraud, Philippe Dal Santo

LAMPA, ENSAM, 2 Boulevard du Ronceray, 49035 Angers, Cedex 01, France

Keywords:
AA5383 alloy
High temperature behavior
BBC 2003 yield function
MMC damage criterion

Associate Editor: Z Cui

A B S T R A C T

Because of its excellent properties, such as good corrosion resistance, high specific strength and important ductility, the AA5383 aluminum alloy is largely employed for naval applications. In this work, the mechanical behavior of the AA5383 alloy at elevated temperatures, which is an important aspect for the control of forming operations, is investigated. For this purpose, an experimental campaign, including uniaxial tension, biaxial tension, and shear tests, is performed to cover an important range of temperatures (623 ~ 723 K) and strain rates ($10^{-4} \sim 10^{-1}$ s^{-1}). A constitutive model for the description of the high temperature behavior of the AA5383 alloy is then proposed. For the deformation behavior, this model combines a viscoplastic flow rule with the BBC2003 anisotropic yield criterion. Also, the prediction of ductile fracture, which is an important aspect for formability, relies on an extended version of the modified Mohr-Coulomb criterion. The extension allows including the impact of temperature and strain rate on ductile fracture *as well as a cut-off value for stress triaxiality*. Finally, numerical simulations of the experimental tests are performed to identify the flow rule, yield criterion and fracture criterion parameters by combining different optimization methods. The numerical and experimental results of the different tests are in good agreement, which indicates that the proposed constitutive model is well suited for investigating the impact of process conditions on the formability of the AA5383 alloy at high temperatures.

1. Introduction

Due to the excellent properties, such as good corrosion resistance, high specific strength and important ductility, 5xxx aluminum alloys are extensively applied in the automotive and marine industries. For marine applications, the AA5083 and AA5383 alloys are the most commonly used wrought aluminum alloys. The deformation and fracture behaviors of the AA5083 alloy have been extensively investigated. Naka et al. (2001) studied the formability of an AA5083 alloy sheet at high temperatures. The results showed that the lower speed can lead to the higher forming limit strain for temperatures ranging between 423 and 573 K, while the forming limit diagram is not affected by the speed at room temperature. Kaibyshev et al. (2005) discussed the deformation behavior of a AA5083 aluminum alloy with Zr and Mn *additions* in the temperature range of 523 ~ 843 K for different strain rates. They found that the threshold stress tends to disappear for high temperatures ($T > 773$ K). Magee and Ladani (2013) also studied the deformation behavior of the AA5083 alloy with different initial microstructures. The AA5383 alloy is quite similar to the AA5083 alloy, except that the chemical composition has been adjusted to increase the strength of welded structures and improve corrosion resistance (Raynaud and Gomiero, 1997). However, few researches have been dedicated to the deformation behavior of the AA5383 alloy, especially at high temperatures, though this aspect is important for the control of forming processes.

To investigate the formability of metallic alloys at high temperatures, numerical simulation is often used to optimize process conditions (Jarrar et al., 2010). The obtained results are only reliable when the material behavior is appropriately described. For this purpose, constitutive equations have to include the influence of temperature and strain rate on the flow behavior. These equations are usually classified into physics-based and phenomenological models. For physics-based models, the construction of constitutive relations uses some variables with an explicit physical meaning (e.g. dislocation densities) to connect the flow stress to the strain rate and temperature (Kocks, 1975). On the other hand, phenomenological models, for which a partial review has been proposed by Sung et al. (2010), directly describe the effect of temperature, strain and strain rate on the deformation behavior. Though they do not provide information about the evolution of the microstructure, phenomenological models are widely used due to their

* Corresponding author.
E-mail address: rou.du@ensam.eu (R. Du).

https://doi.org/10.1016/j.jmatprotec.2020.116609

ease of identification and implementation. For instance, Grujicic et al. (2011) have used a modified version of the Johnson-Cook model to describe the flow behavior of the AA5083 alloy.

For sheet forming processes, failure prediction is also an important aspect to be considered. Different fracture models, in either coupled or uncoupled forms, have been proposed. For coupled approaches, fracture models consider the impact of damage on the deformation behavior, which render difficult the calibration of material parameters (Teng et al., 2017). At the opposite, the influence of the damage evolution on the yield surface is neglected by uncoupled approaches. For uncoupled models, fracture occurs when a damage variable, which usually depends on the equivalent plastic strain and stress state (Li et al., 2011), reaches a critical value. For instance, Cockcroft and Latham (1968) proposed a simple damage criterion, which uses the maximum principal stress, to predict the fracture initiation position. Oyane (1972) included the influence of the mean stress in a ductile fracture criterion. The impact of temperature and strain rate on the fracture behavior has been incorporated in the ductile fracture criterion of Johnson and Cook (1985). More recently, a modified version of Mohr-Coulomb fracture criterion has been proposed by Bai and Wierzbicki (2010) to predict the damage behavior of metallic alloys. The fracture behavior for shear-dominated loading modes has been the subject of some recent studies (Hu et al., 2017) that lead to the development of some specific fracture criteria (Mohr and Marcadet, 2015). Also, a ductile fracture criterion motivated by the physical mechanisms of nucleation, growth and shear coalescence of voids has been developed by Lou et al. (2012). It has later been modified by Lou et al. (2014) to consider the impact of the Lode angle, temperature and strain rate on the cut-off value for stress triaxiality. Qian et al. (2017) adopted the modified Mohr-Coulomb (MMC) criterion to model the ductile fracture of AA5083-O alluminum alloy. They found that this criterion can correctly predict fracture for both tension-dominated and shear-dominated loading modes.

This study aims at proposing a constitutive model to describe both the deformation and fracture behaviors of the AA5383 alloy at high temperatures under plane stress conditions. For this purpose, tension tests are performed at different strain rates ($10^{-4} \sim 10^{-1}$ s^{-1}) and temperatures (623 ~ 723 K). These conditions correspond to the typical strain rate and temperature ranges for the sheet forming processes of AA5xxx alloys (Liu et al., 2010). The fracture behavior is then investigated by performing tension, shear and free bulging tests. Based on the experimental dataset, a constitutive model is proposed for the AA5383 alloy. For the flow behavior, the model uses the anisotropic yield criterion of Banabic (2005) together with a viscoplastic flow rule. The modified Mohr-Coulomb criterion (Bai and Wierzbicki, 2010), which includes temperature and strain rate effects, is selected to predict the ductile fracture. The corresponding parameters are identified for the AA5383 alloy from the fracture strains determined from different deformation paths.

2. Experimental procedures

2.1. Material description

This study focuses on the AA5383 aluminum alloy. The detailed chemical composition is shown in Table 1. The studied alloy has been delivered in the form of 3.2 mm thick sheets. To characterize the behavior of this alloy, different specimens have been machined from the sheet. To increase ductility, specimens have been held at 623 K for 5 min prior to deformation. The corresponding microstructure is shown in Fig. 1(a). It is composed of equiaxed grains with a mean size of 19 μm. Also, some X-ray diffraction analyses have been performed to measure the {111}, {002}, {220} and {311} pole figures of the heat-treated AA5383 alloy. Based on the results, the inverse pole figures associated with the normal (ND) and rolling (RD) directions of the sheet have been computed (see Fig. 1(b–c)). According to the results, the heat-treated AA5383 alloy likely exhibits significant plastic deformation anisotropy due to the presence of important cube and brass texture components.

2.2. Specimen geometries

To investigate the mechanical behavior of the AA5383 alloy at high temperatures, different tests have been performed. These tests aim at characterizing both the deformation behavior and the fracture response over a wide range of temperature and strain rate. For this purpose, the following specimens have been machined from AA5383 sheets (see Fig. 2):

- Uniaxial Tension (UT) specimens to characterize the flow behavior. The loading direction is aligned with an angle of either 0°, 45° or 90° with respect to rolling direction.
- *Uniaxial Compression (UC) specimens to characterize the fracture behavior for negative triaxialities. The loading direction is aligned with the rolling direction.*
- Eccentric shear (SH) specimens with two asymmetric notches to study the fracture behavior for a purely deviatoric stress state. The geometry of these specimens is developed from the work of Peirs et al. (2012). The loading direction coincides with the rolling direction.
- *Central hole (CH) specimens with radius $R = 6$ mm to characterize the fracture behavior under uniaxial tension stress state. The loading direction is aligned with the rolling direction.*
- Notched Tension (NT) specimens to characterize the fracture behavior for different triaxiality values. NT specimens have been machined with different circular cut-out radii: $R = 20$ mm (NT20), $R = 10$ mm (NT10) and $R = 5$ mm (NT5). The loading direction coincides with the rolling direction.
- Free Bulging (FB) flanges with a diameter of 290 mm to characterize the mechanical behavior for a biaxial stress state.

2.3. Experimental set-up for tension and shear tests

Except from free bulging tests, all tests have been carried out on a GLEEBLE 3500 machine equipped with a 100 kN load cell. Specimens are fixed between two copper jaws, which are cooled with a water circuit. Prior to deformation, specimens are first heated to the studied temperature by using the Joule effect. The temperature is measured by a K-type thermocouple. Tests are performed under vacuum conditions to limit oxidation at high temperatures. *For uniaxial tension tests, the elongation is measured by an axial extensometer with an initial gauge length of 10 mm. Some preliminary tests with multiple thermocouples have been conducted to ensure that thermal gradients within the effective gauge region of uniaxial tension specimens are negligible.* In some cases, a transverse extensometer has been placed on the specimens to measure the transverse strain. *For notched and shear specimens, the initial gauge length for the axial extensometer is 25 mm. While the initial gauge length for compression specimens is 6 mm.*

To characterize the flow resistance at high temperatures, some

Table 1
Chemical composition of AA5383 alloy (wt. %).

Material	Mg(%)	Mn(%)	Fe(%)	Cr(%)	Si(%)	Cr(%)	Cu(%)	Zn(%)	Al
AA5383	4.91	0.80	0.17	0.12	0.05	0.12	0.06	0.04	balance

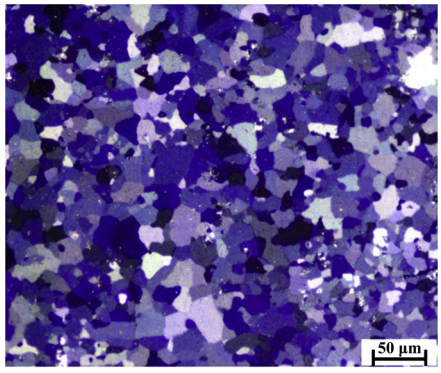

(a)

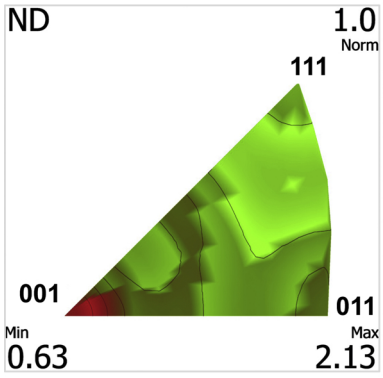

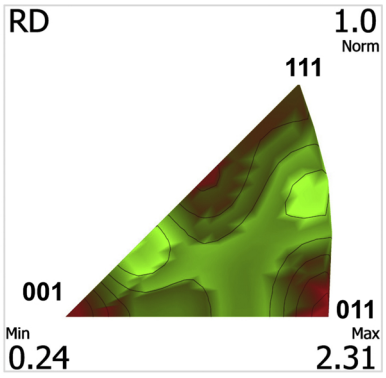

(b) (c)

Fig. 1. AA5383 alloy sheet after heat treatment at 623 K for 5 min: (a) Metallographic observations, (b) inverse pole figure for the normal direction (ND) and (c) inverse pole figure for the rolling direction (RD).

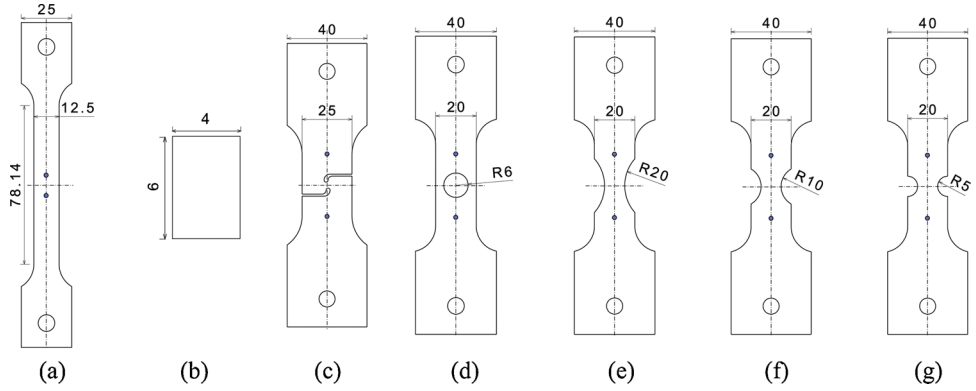

Fig. 2. Different shapes of specimen used for experimental characterization: (a) UT specimen; (b) UC specimen; (c) SH specimen; (d) CH specimen; (e) NT20 specimen; (f) NT10 specimen and (g) NT5 specimen. Blue slid dots highlight the position of the extensometer for relative displacement measurement. (For interpretation of the references to colour in this figure legend, the reader is referred to the web version of this article).

uniaxial tension tests have been carried out at different temperatures (623, 673 and 723 K) and true strain rates (0.0001, 0.001, 0.01, 0.1 s^{-1}) along the rolling direction. Also, to investigate plastic deformation anisotropy, some uniaxial tension specimens have been deformed along the 0°, 45° and 90° directions at 673 K and 0.001 s^{-1}. For these tests, both the axial and transverse strains have been measured to obtain the corresponding Lankford coefficients r_0, r_{45} and r_{90}.

To evaluate the impact of the stress state on the fracture behavior, some *UC, SH, CH,* NT20, NT10 and NT5 specimens have been deformed at 673 K under displacement control for different velocities of 0.0055, 0.004, 0.0025, 0.011, 0.008 and 0.006 mm/s, respectively. These velocities have been selected to obtain an average equivalent strain rate of 0.001 s^{-1} at the critical position. To investigate the influence of temperature on the fracture behavior, some NT20 specimens have been deformed with a fixed equivalent strain rate of 0.001 s^{-1} for different temperatures (623, 673 and 723 K). In a similar fashion, the influence of the strain rate has been evaluated with some NT20 specimens that have been deformed at a fixed temperature of 673 K for different strain rates (0.0001, 0.001, 0.01, 0.1 s^{-1}). All the aforementioned tests have been performed three times to check repeatability.

2.4. Experimental set-up for free bulging tests

Free bulging tests have been carried out to evaluate the mechanical

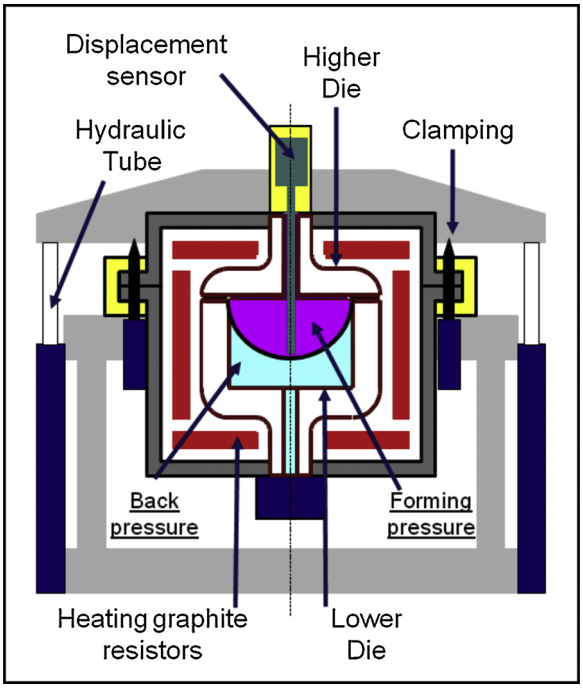

Fig. 3. Schematic diagram of the gas forming machine.

behavior of the AA5383 alloy under a biaxial stress state. A gas forming machine, which is schematically presented in Fig. 3, has been used for these tests.

To perform a biaxial test, the specimen is first clamped between the blank holder and the matrix. Using graphite resistors, the temperature of the tooling and the specimen is then increased to the deformation temperature, which is controlled with a K-type thermocouple placed at the center position of the specimen. Finally, argon gas is injected to inflate the specimen. The input pressure is controlled either according to the height of the deformed specimen or according to the forming time. The height of the dome apex is measured with a displacement sensor, which is located outside the hot zone. A ceramic bar, attached to the end of the sensor, is used to measure the pole displacement by direct contact.

For anisotropic materials, the flow behaviors for uniaxial tension and biaxial tension are generally different (Aksenov et al., 2016). As the stress state during forming operations is generally complex, obtaining an accurate value of the biaxial yield stress is of great importance. For this purpose, some free bulging tests have been carried out with the gas forming machine to estimate the biaxial yield stress at 673 K. Three constant forming pressures have been selected at 673 K: $P_1 = 0.6$ MPa, $P_2 = 1.0$ MPa and $P_3 = 1.5$ MPa. However, unlike uniaxial tension experiments, the biaxial yield stress cannot be directly determined from the experimental data. To overcome this difficulty, an inverse method will later be used to estimate the biaxial yield stress.

Also, for the estimation of the fracture strain under biaxial tension, a free bulging test has been carried out at 673 K and 0.001 s^{-1} until fracture was detected. To control the strain rate in the experiment, the evolution of the forming pressure has been determined numerically prior to the bulging test. The employed constitutive model and pressure law are presented in the following sections.

3. Experimental results

3.1. Plastic deformation behavior

The relations between the true axial stress and strain for different

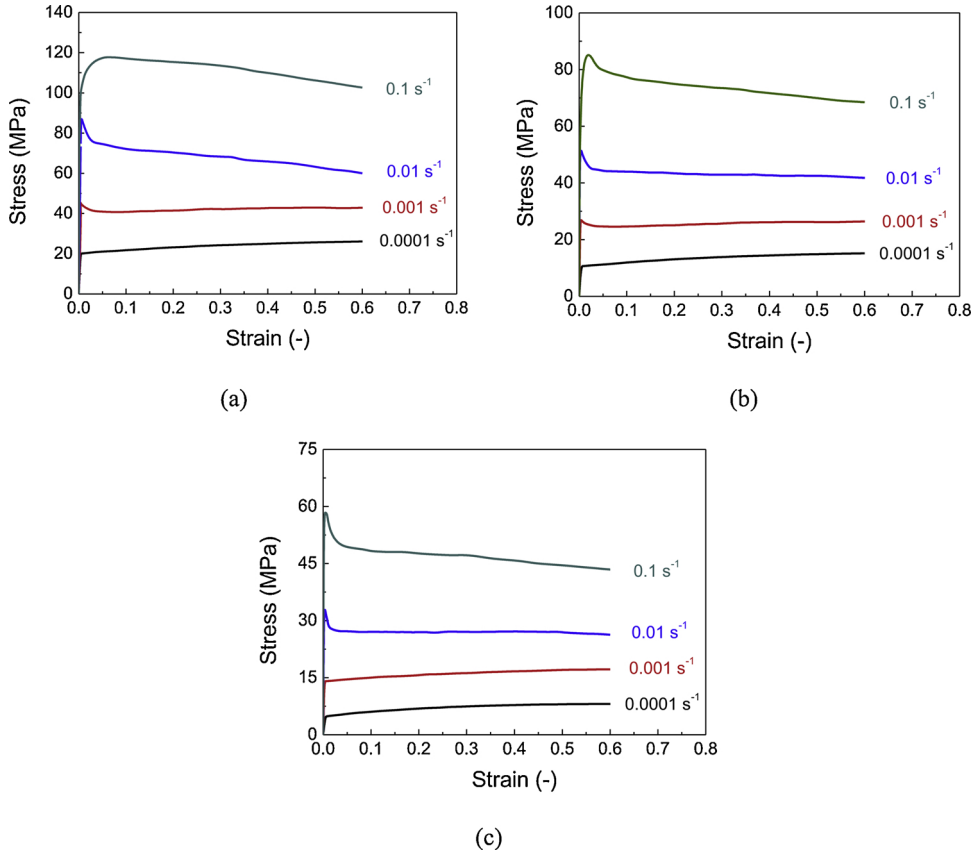

Fig. 4. Uniaxial flow stress in the rolling direction at different temperatures: (a) 623 K; (b) 673 K and (c) 723 K.

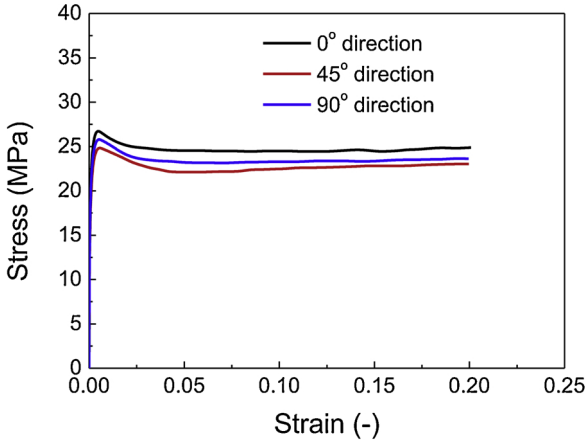

Fig. 5. Uniaxial flow stress curves in different loading directions at 673 K and 0.001 s^{-1}.

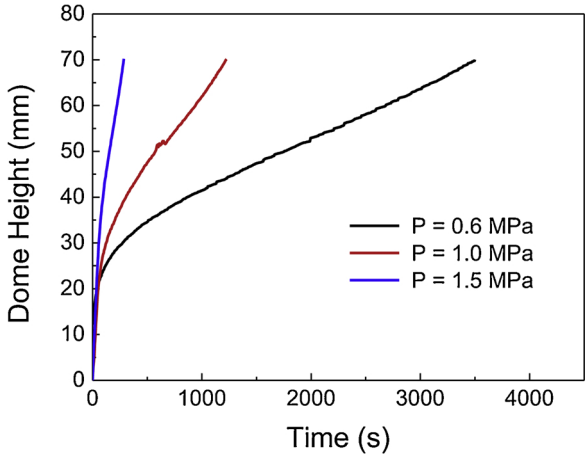

Fig. 6. Evolution of the dome height for FB tests under different constant forming pressures.

Table 2
Yield stresses and Lankford coefficients at 673 K and 0.001 s^{-1}.

r_0[-]	r_{45}[-]	r_{90}[-]	Y_0[MPa]	Y_{45}[MPa]	Y_{90}[MPa]
0.71	0.88	0.78	26.8	24.7	25.7

deformation temperatures and strain rates are shown in Fig. 4. It should be noticed that uniaxial tension tests have been conducted up to a maximum axial strain of 60 %, so that necking does not occur. Only the uniform elongation stage is therefore considered for the investigation of the flow behavior under uniaxial tension. From the experimental results, the flow behavior is significantly influenced by the temperature and strain rate. Generally, the steady stress and yield stress increase with the decrease of temperature and the increase of strain rate. A yield drop phenomenon, which corresponds to the rapid decrease of the flow stress at the onset of plastic deformation, is observed in a certain range of temperatures and strain rates. This phenomenon is likely explained by the sudden increase of the mobile dislocation density at the beginning of deformation (Voyiadjis and Abed, 2005). Also, whatever the deformation temperature is, a hardening behavior is observed at low strain rates while softening is predominant for high strain rates. Some metallographic observations of deformed specimens have shown that the grain size is largely reduced after deformation at high strain rates (i.e. $\dot{\bar{\varepsilon}}^P \geq 0.01\ s^{-1}$). These results indicate that the softening behavior, which is important for high strain rates, is likely explained by dynamic recrystallization. A similar recrystallization phenomenon has been observed for the AA5083 alloy at high temperature by Agarwal et al. (2008)

The stress-strain curves obtained for different loading directions (i.e. 0°, 45° and 90°) at 673 K and 0.001 s^{-1} are plotted in Fig. 5. According to the results, the AA5383 alloy exhibits an anisotropic plastic deformation behavior. The rolling direction displays the highest yield stress compared with the other two directions. *The yield stresses for uniaxial tension, which have been determined at the onset of plastic yielding, are listed in* Table 2. *The calculated Lankford coefficients, which have been measured for an axial strain of 15 %, are also given*. Following the general trend for aluminum alloys, the Lankford coefficients are generally lower than unity (Driver and Engler, 2004). Also, the Lankford coefficients of the present AA5383 alloy are very similar to those obtained for Al-Mg alloys at elevated temperatures (Naka et al., 2003).

The experimental dome height evolutions for free bulging (FB) tests under three constant forming pressures at 673 K are presented in Fig. 6. All the tests have been stopped at a dome displacement of 70 mm. The displacement rate at the dome apex is very high at the beginning and progressively tends to a steady regime with a constant value. To the same extent of deformation, the highest pressure allows reducing the forming time significantly. These experimental results will be used in the following to estimate the biaxial yield stress Y_b at 673 K and 0.001 s^{-1}.

3.2. Fracture behavior

The force versus displacement curves obtained from shear (SH), tension (CH) and notched tension (NT) tests performed at 673 K and 0.001 s^{-1} are shown in Fig. 7. For shear tests, the force progressively increases during the deformation process until fracture initiates. The drop of the axial force is therefore considered as the starting point of fracture. Unlike shear tests, for central hole and notched tension specimens, the axial force decreases at the beginning of the plastic deformation. In the following, the sudden drop of axial force is considered as the point of fracture initiation. Also, with the same initial gauge area, the axial forces for the different notched specimens at the onset of plastic deformation are quite close to each other. For the fracture elongation of notched specimens, NT20 specimens exhibit the maximum displacement (around 7 mm). Due to the impact of triaxiality, the fracture elongation decreases with the reduction of cut-out radii values for notched specimens (Gao et al., 2011). For uniaxial compression tests, whatever the strain rate is, no fracture has been detected before significant barreling of specimens occurs.

Some images of notched tension specimens at the instance of failure are shown in Fig. 8. The position of failure initiation changes from the center to the edge as the notch radius decreases. Specifically, for NT20 and NT10 specimens, the fracture initiates from the center of specimen. The failure of NT5 specimens is simultaneously detected in the center and on the edges. A similar phenomenon for notched tension tests has been observed by Majzoobi et al. (2018) for the AA2024 alloy.

At each testing temperature and strain rate for NT20 specimens, there exists high repeatability for force-displacement curves before the sudden decrease of axial force (seen in Fig. 9). As expected, the fracture displacement increases with the increment of temperature and the decrement of strain rate.

The dome height evolution for a free bulging test with a constant strain rate of 0.001 s^{-1} at the dome apex is presented in Fig. 10(a). *To control the strain rate, the algorithm of* Jarrar et al. (2010) *has been used. This algorithm consists in calculating the ratio γ between maximum strain rate in the sheet and the target strain rate. The pressure is then controlled with the following relation:*

$$p_{new}/p_{old} = \begin{cases} 2.43 & \gamma < 0.3 \\ -10\log_{10}^{3}(\gamma) + 1 & 0.3 \leq \gamma < 1.26 \\ 0.99 & \gamma \geq 1.26 \end{cases} \quad (1)$$

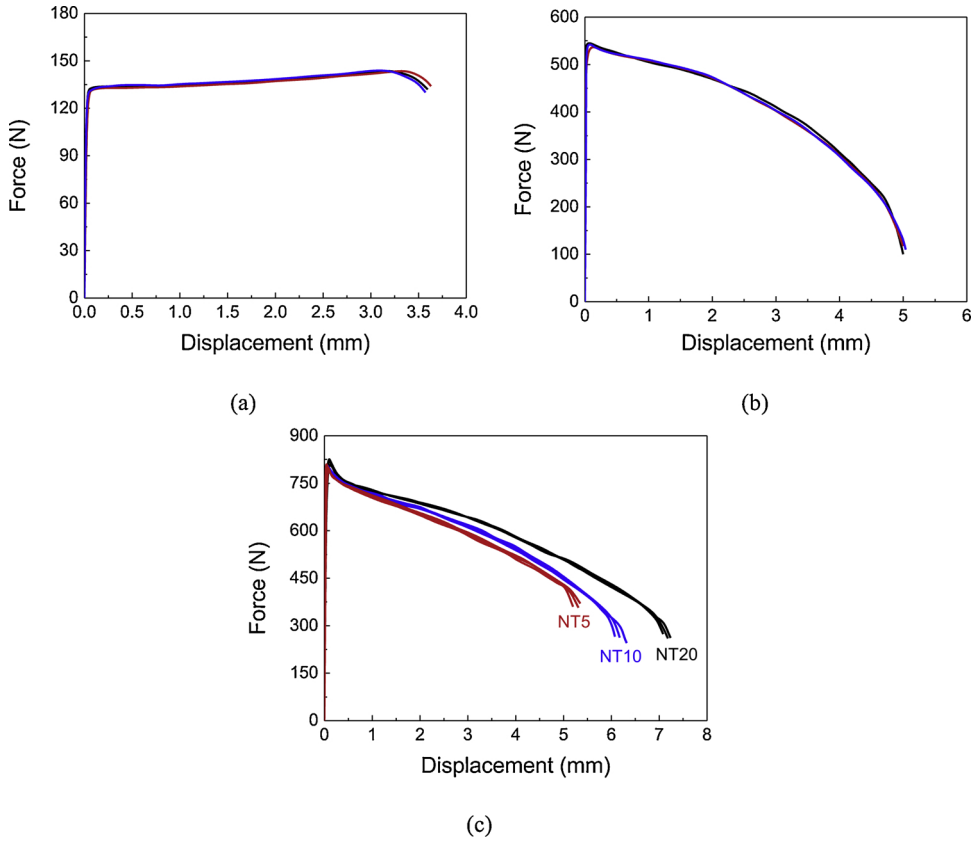

Fig. 7. Force-displacement curves obtained at 673 K and 0.001 s^{-1} for: (a) shear specimens; (b) central hole tension specimens and (c) notched tension specimens.

where p_{old} is the pressure at the previous step of the numerical simulation, p_{new} is the pressure at the current step. This algorithm allows determining the temporal evolution of the pressure. The pressure evolution determined from the numerical simulation has then been used as an input of the bulging test with constant strain rate. According to the experimental results, the dome displacement increases gradually with the forming time up to a maximum value of 82.2 mm, which is the fracture displacement for the free bulging test at 673 K and 0.001 s^{-1}.

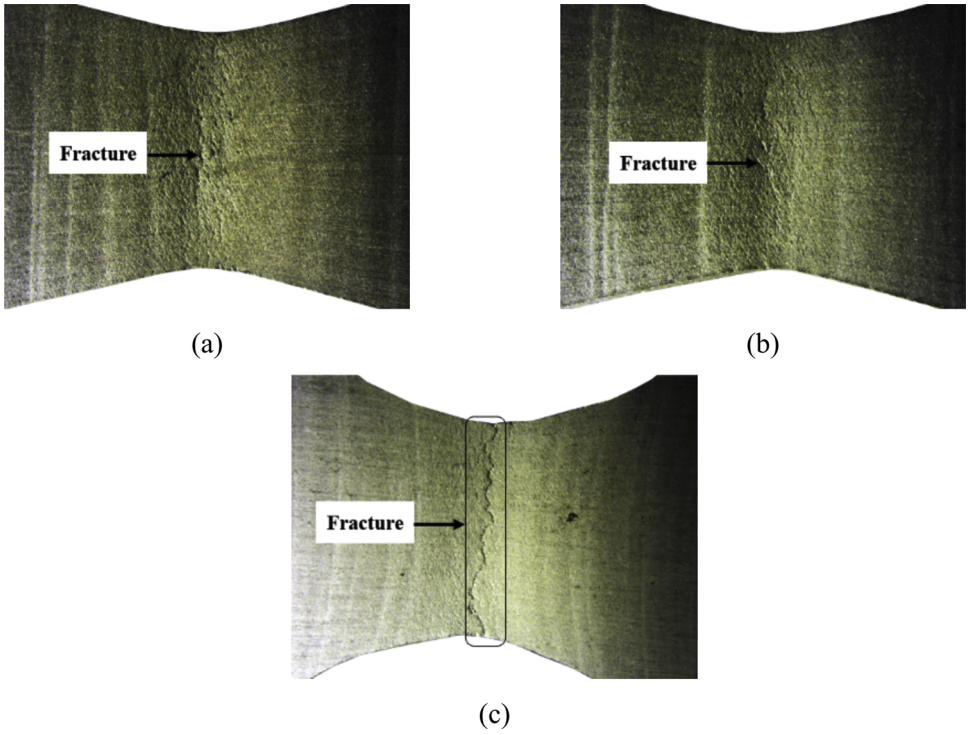

Fig. 8. Fracture initiation for different notched tension specimens deformed at 673 K and 0.001 s^{-1}: (a) NT20 specimen, (b) NT10 specimen and (c) NT5 specimen.

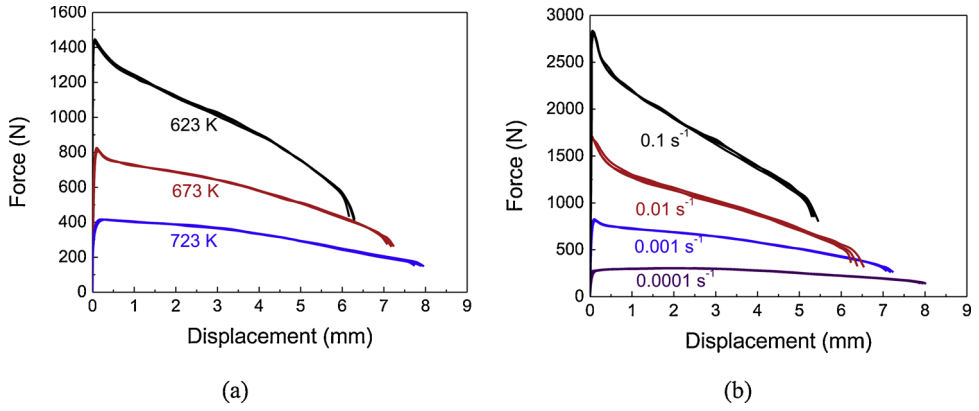

Fig. 9. Force-displacement curves for NT20 specimen deformed at (a) 0.001 s^{-1} and (b) 673 K.

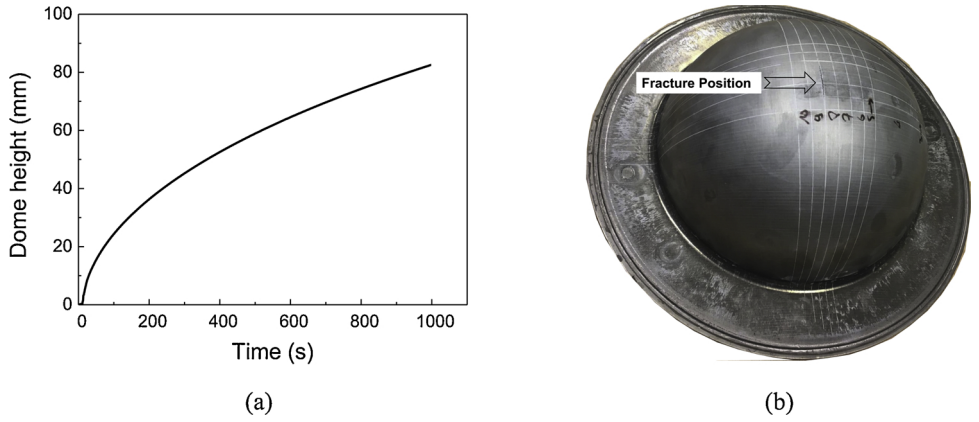

Fig. 10. (a) Dome height-time curves obtained from FB tests at 623 K and 0.001 s^{-1} and (b) deformed specimen.

The deformed specimen is shown in Fig. 10(b). We can see that the fracture is located near the dome apex.

4. Constitutive model

A constitutive model, which is used to describe the hot deformation behavior of the AA5383 alloy, is presented in this section. The proposed model uses the framework of rate-dependent plasticity to include the impact of temperature and strain rate on the flow behavior and a phenomenological damage criterion to consider ductile fracture.

4.1. Flow rule and yield criterion

To determine whether the conditions for plastic flow are met or not, the present model uses a yield function Φ that relates the equivalent stress $\bar{\sigma}$ to the equivalent plastic strain $\bar{\varepsilon}^P$, the equivalent plastic strain rate $\dot{\bar{\varepsilon}}^P$ and the temperature θ. Hardening is assumed to be purely isotropic and neither kinematic nor distortional hardening is considered for simplicity. Further experimental work would have to be conducted to determine the exact nature of the hardening behavior (e.g. isotropic, kinematic) of the AA5383 alloy. For the present application, the type of hardening is not expected to be an important aspect of the constitutive model because the hardening behavior is not significant. With these assumptions, the yield function takes the following form:

$$\Phi(\bar{\sigma}, \bar{\varepsilon}^P, \dot{\bar{\varepsilon}}^P, \theta) = \bar{\sigma} - Y[\bar{\varepsilon}^P, \dot{\bar{\varepsilon}}^P, \theta] = 0 \tag{2}$$

In the above equation, Y is the instantaneous yield stress. In order to consider plastic deformation anisotropy, the BBC2003 yield criterion (Banabic, 2005) has been selected. Banabic (2005) expressed the equivalent stress $\bar{\sigma}$ under plane stress conditions by:

$$\bar{\sigma}(a, M, N, P, Q, R, S, T, k, \boldsymbol{\sigma}) = [a(\Gamma + \Psi)^{2k} + a(\Gamma - \Psi)^{2k} + (1 - a)(2\Lambda)^{2k}]^{\frac{1}{2k}} \tag{3}$$

where $\boldsymbol{\sigma}$ is the stress tensor, k and a are material parameters. The yield locus is convex when k is a positive integer and $0 \leq a \leq 1$. The functions Γ, Ψ and Λ are given by:

$$\begin{aligned} \Gamma &= \frac{\sigma_{11} + M\sigma_{22}}{2} \\ \Psi &= \sqrt{\frac{(N\sigma_{11} - P\sigma_{22})^2}{4} + Q^2\sigma_{12}\sigma_{21}} \\ \Lambda &= \sqrt{\frac{(R\sigma_{11} - S\sigma_{22})^2}{4} + T^2\sigma_{12}\sigma_{21}} \end{aligned} \tag{4}$$

In the above equations, a, M, N, P, Q, R, S and T are the yield criterion parameters. The integer parameter k is related to the crystallographic structure of the material. For FCC materials, such as the AA5383 alloy, the recommended value of this exponent is $k = 4$ (Banabic, 2005).

Similarly to the constitutive model proposed by Johnson and Cook (1983), the following multiplicative decomposition of the yield stress Y is adopted:

$$Y[\bar{\varepsilon}^p, \dot{\bar{\varepsilon}}^p, \theta] = Y_{\bar{\varepsilon}^p}[\bar{\varepsilon}^p] Y_{\dot{\bar{\varepsilon}}^p}[\dot{\bar{\varepsilon}}^p] Y_{\theta}[\theta] \tag{5}$$

The contribution of strain hardening is denoted by $Y_{\bar{\varepsilon}^p}[\bar{\varepsilon}^p]$. The above equation is independently scaled by a temperature term $Y_{\theta}[\theta]$ and a strain rate term $Y_{\dot{\bar{\varepsilon}}^p}[\dot{\bar{\varepsilon}}^p]$. In the present work, strain hardening is described with a modified Swift law:

$$Y_{\bar{\varepsilon}^p}[\bar{\varepsilon}^p] = K(\bar{\varepsilon}^P + \bar{\varepsilon}_0^P)^n \exp(-b\bar{\varepsilon}^P) \tag{6}$$

where K, $\bar{\varepsilon}_0^P$, n and b are the strain hardening parameters. Following the suggestion of Johnson and Cook (1983), the contributions of

temperature and equivalent strain rate to the yield stress are given by:

$$Y_{\dot{\bar{\varepsilon}}^P}[\dot{\bar{\varepsilon}}^P] = (\dot{\bar{\varepsilon}}^P)^m \tag{7}$$

and

$$Y_{\theta}[\theta] = 1 - \left\{\frac{\theta - \theta_{ref}}{\theta_m - \theta_{ref}}\right\}^{\beta} \tag{8}$$

where m represents the strain-rate sensitivity; θ_{ref} and θ_m refer to the reference and melting temperatures, respectively; β is the temperature sensitivity parameter.

4.2. Ductile fracture criterion

Based on the Mohr-Coulomb fracture approach, Bai and Wierzbicki (2010) have proposed a modified version of the classical damage criterion for ductile materials. In the special case of a plane stress state, this modified Mohr-Coulomb (MMC) criterion only depends on the stress triaxiality η (Li et al., 2010). The stress triaxiality is defined by the ratio between the mean stress and the von Mises equivalent stress. The fracture strain $\bar{\varepsilon}_f^P$ in the MMC criterion is represented by:

$$\bar{\varepsilon}_f^P(\eta)_{MMC} = \{\frac{A}{c_2} f_3 [\sqrt{\frac{1+c_1^2}{3}} f_1 + c_1(\eta + \frac{f_2}{3})]\}^{-\frac{1}{n'}} \tag{9}$$

with

$$\begin{aligned} f_1 &= \cos\{\frac{1}{3}\arcsin[-\frac{27}{2}\eta(\eta^2 - \frac{1}{3})]\} \\ f_2 &= \sin\{\frac{1}{3}\arcsin[-\frac{27}{2}\eta(\eta^2 - \frac{1}{3})]\} \\ f_3 &= c_3 + \frac{\sqrt{3}}{2-\sqrt{3}}(c_\theta^{ax} - c_3)(\frac{1}{f_1} - 1) \end{aligned} \tag{10}$$

where A and n' are two hardening factors, c_1, c_2 and c_3 are three fracture parameters. The value of c_θ^{ax} is selected based on the type of test used for calibrating the strain hardening function (Bai and Wierzbicki, 2008). In the present case, uniaxial tension tests are used so $c_\theta^{ax} = 1$.

The MMC criterion presented here has two drawbacks. First, it is limited to the condition of cold deformation. To account for the impact of temperature and strain rate, two methods are commonly used. The first method consists in considering the parameters of the original MMC to be dependent on temperature and strain rate. For the second method, which has been adopted by Johnson and Cook (1985), a strain rate and a temperature scaling factors are introduced in the expression of the fracture strain. In our study, the later method is used. Second, the MMC criterion does not provide realistic estimations of fracture strains at low stress triaxialities. To include a cut-off value for stress triaxiality, a third scaling factor has been introduced. This scaling factor is such that the fracture strain is infinite when the stress triaxiality is inferior to some critical value η_{cutoff}. The MMC criterion under plane stress conditions can thus be extended as follows:

$$\bar{\varepsilon}_f^P(\eta, \dot{\bar{\varepsilon}}^P, \theta) = \bar{\varepsilon}_f^P(\eta)_{MMC}[1 + D_1 \ln \dot{\bar{\varepsilon}}^*][1 + D_2\theta^*]\exp\left\{\frac{Z}{\langle \eta - \eta_{cutoff}\rangle}\right\} \tag{11}$$

In the above expression for the fracture strain, Z is a material parameter controlling the transition from the low stress triaxiality region ($\eta \le \eta_{cutoff}$) to the medium and high stress triaxiality region ($\eta > \eta_{cutoff}$). In our case, a constant cut-off value of -1/3 has been selected for the ductile fracture criterion according to the work of Bao and Wierzbicki (2005). This is consistent with our experimental observations showing that no fracture has been detected for uniaxial compression tests. It should however be mentioned that the cut-off value may be depend on the Lode angle, strain rate and temperature (Lou et al., 2014). These effects have been ignored here for the purpose of simplicity. D_1 and D_2 are the parameters related to the strain rate and the temperature influence, respectively. The normalized strain rate $\dot{\bar{\varepsilon}}^*$ is the ratio between the equivalent plastic strain rate $\dot{\bar{\varepsilon}}^P$ and the reference strain rate $\dot{\bar{\varepsilon}}_{ref}$ while the normalized temperature θ^* is defined by:

$$\theta^* = \frac{\theta - \theta_{ref}}{\theta_m - \theta_{ref}} \tag{12}$$

The above expression of the fracture strain is applicable only for monotonic loading paths. For complex loading paths, a linear cumulative damage rule is adopted. A damage variable D is therefore introduced to determine whether the conditions for ductile fracture are met or not. For a given deformation path, the damage variable D is given by:

$$D(\bar{\varepsilon}^P) = \int_0^{\bar{\varepsilon}_f^P} \frac{d\bar{\varepsilon}^P}{\bar{\varepsilon}_f^P(\eta, \dot{\bar{\varepsilon}}^P, \theta)} \tag{13}$$

A material point is considered to fail when the damage variable reaches a unit value.

5. Parameter identification

The parameters of the constitutive model are listed in Table 3. The procedure used for determining those parameters for the AA5383 alloy is detailed in the following.

5.1. Identification strategy

The general strategy for parameter identification is presented in Table 3. First, the flow rule parameters have been determined from the uniaxial tension tests performed along the rolling direction. *For this purpose, a genetic algorithm (GA) has been used to estimate the corresponding parameters. Unlike some other common optimization methods (e.g.*

Table 3
Parameter identification strategy for the AA5383 alloy.

	Parameters	Experimental data	Testing condition	Identification method
Flow rule	K, $\bar{\varepsilon}_0^P$, n, m, b, β	Uniaxial Tension (UT)	T: 623 ~ 723 K $\dot{\bar{\varepsilon}}$: 0.0001 ~ 0.1 s^{-1} Loading direction: 0°	GA method
Yield criterion	a, M, N, P, Q, R, S, T	Uniaxial Tension (UT) Free Bulging (FB)	*For UT:* T: 673 K; $\dot{\bar{\varepsilon}}$: 0.001 s^{-1} Loading direction: 0°, 45°, 90° *For FB:* T: 673 K; $\dot{\bar{\varepsilon}}$: 0.001 s^{-1}	Direct method + Inverse method + Newton-Raphson method
Damage criterion	A, c_1, c_2, c_3, n', D_1, D_2, Z	Tension (CH and NT) Shear (SH) Free Bulging(FB)	*For CH, NT, SH, FB:* T: 673 K; $\dot{\bar{\varepsilon}}$: 0.001 s^{-1} ; *For NT20:* T: 623, 673, 723 K $\dot{\bar{\varepsilon}}$: 0.0001, 0.001, 0.01, 0.1 s^{-1}	Inverse method + GA method

Table 4
Flow rule parameters for the AA5383 aluminum alloy.

K[MPa]	$\bar{\varepsilon}_0^P$[-]	n[-]	m[-]	b[-]	β[-]
480	0.82	0.65	0.24	0.60	0.28

*Newton-Raphson, Levenberg-Marquardt), genetic algorithms have some ability to overcome the difficulties associated with local minima (*Skippon et al., 2012*)*

Then, to adjust the yield criterion parameters, the yield stresses associated with different loading modes must be known. For uniaxial tension tests, the yield stresses corresponding to the different loading directions are directly obtained from the experimental data. At the opposite, the yield stress for biaxial tension is not directly available from free bulging tests. Therefore, some numerical simulations of bulging tests have been performed to estimate the biaxial yield stress by comparing the numerical and experimental dome height versus time evolutions for the different imposed pressures. A Newton-Raphson method has been used to adjust the yield criterion parameters from the different yield stresses.

Finally, with the identified flow rule and yield criterion, some numerical simulations of the shear, central hole tension, notched tension and free bulging tests have been conducted to determine the MMC fracture criterion parameters. The fracture strains for different loading paths have been estimated from the simulation results. The criterion parameters have been identified from the fracture strains with a genetic algorithm.

5.2. Numerical models

In order to perform the simulations needed for parameter identification, the proposed constitutive model has been implemented within the implicit finite element solver ABAQUS®/Standard. S4 Shell elements are employed with stiffness-based hourglass control. *While shell elements allow reducing the computation time, the necking observed at high temperature for SH and CH specimens may not be correctly depicted.* For simplification, all the simulations have been conducted with the same elastic constants. These values have been set to $E = 30$ GPa and $\nu = 0.335$, which are those given by (Summers et al., 2015) for a temperature of 673 K.

5.3. Flow rule parameters

To estimate the flow rule parameters, a genetic algorithm optimization method (Chen et al., 2012) is employed. In the optimization procedure, the reference temperature is set to $\theta_{ref} = 623$ K, while the melting temperature is $\theta_m = 858$ K. The objective function $\mathfrak{R}_f$ is the relative error between the computed equivalent stress $\bar{\sigma}^C$ and the experimental equivalent stress $\bar{\sigma}^E$:

$$\mathfrak{R}_f(K, \bar{\varepsilon}_0^P, n, m, b, \beta) = \sum \left| \frac{\bar{\sigma}^C - \bar{\sigma}^E}{\bar{\sigma}^E} \right| \tag{14}$$

In our work, the crossover and mutation probability are chosen as 0.8 and 0.02, respectively. The total population consists of 10 000 individuals, and the number of generations is no more than 100. The identified parameters can be found in Table 4.

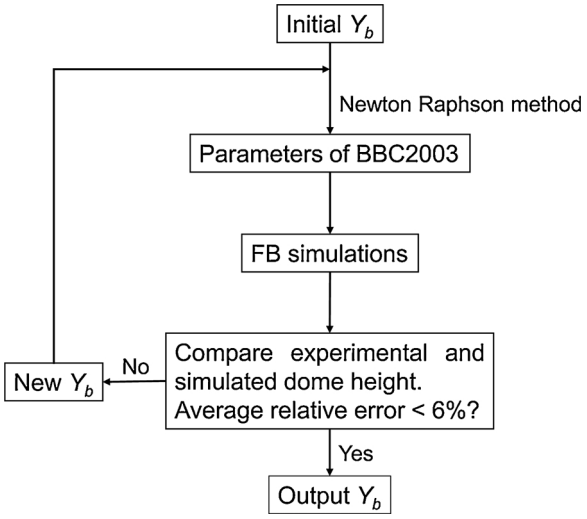

Fig. 11. Flow chart for the BBC2003 criterion identification.

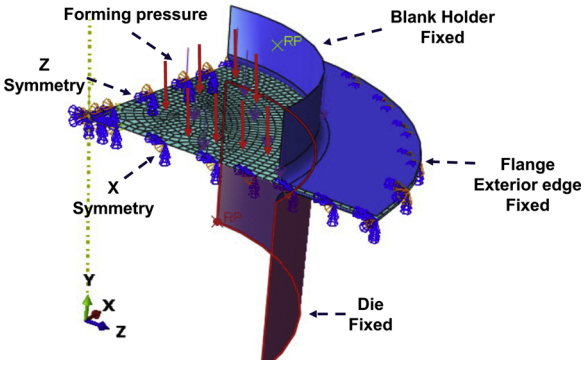

Fig. 12. Numerical model for free bulging simulations.

Table 5
BBC2003 yield criterion parameters for the AA5383 alloy.

a[-]	M[-]	N[-]	P[-]	Q[-]	R[-]	S[-]	T[-]	k[-]
0.0339	1.1254	1.9836	1.9740	2.1624	0.8035	0.8528	0.8867	4

5.4. Yield criterion parameters

Generally, the following experimental data is required to identify the BBC2003 yield criterion:

- The yield stresses Y_0, Y_{45} and Y_{90} for uniaxial tension along the 0°, 45° and 90° directions.
- The Lankford coefficients r_0, r_{45} and r_{90} for uniaxial tension along the 0°, 45° and 90° directions.
- The yield stress Y_b for biaxial tension.
- The Lankford coefficient r_b for biaxial tension.

In this study, the Lankford coefficient r_b for biaxial tension is not

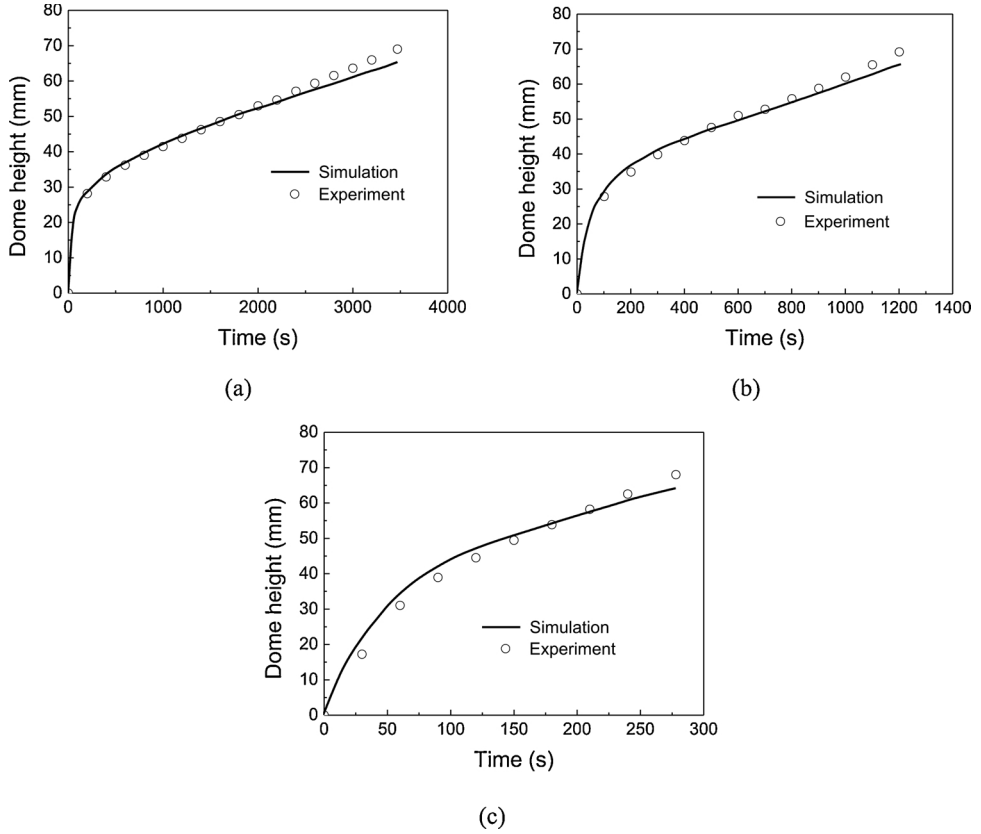

Fig. 13. Experimental and numerical dome height evolutions for forming pressures of 0.6 MPa (a) 1.0 MPa (b) and 1.5 MPa (c).

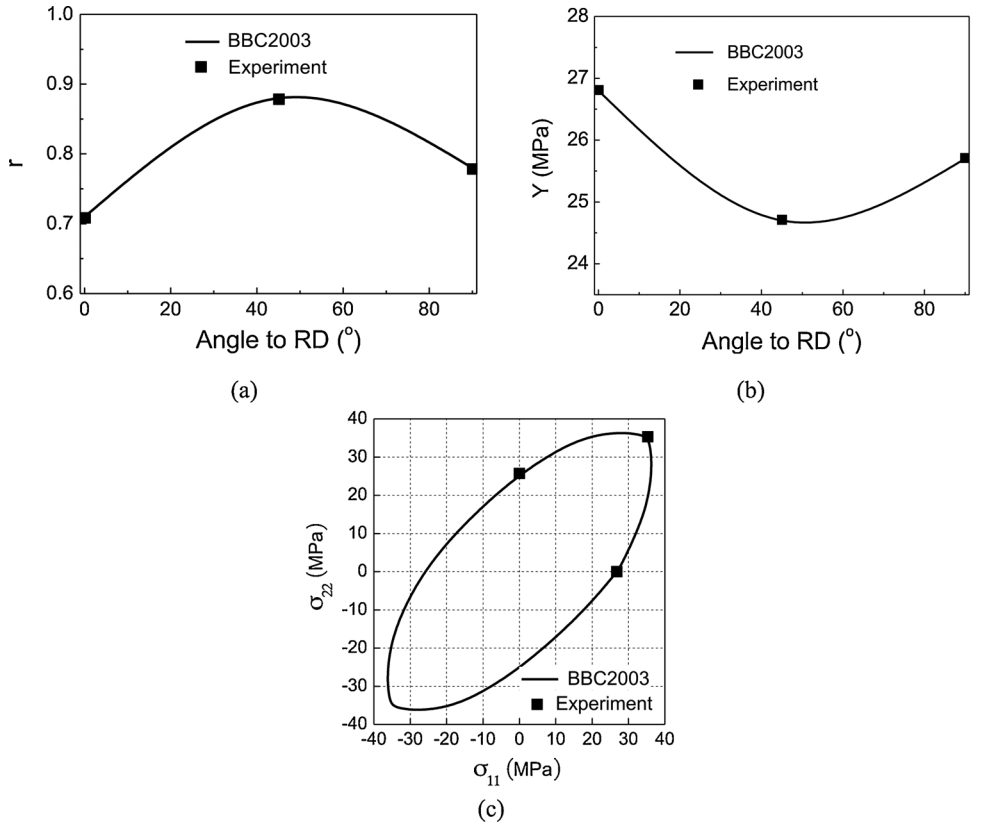

Fig. 14. Comparison of experimental and predicted directional r-values (a), directional yield stresses (b) and yield loci (c).

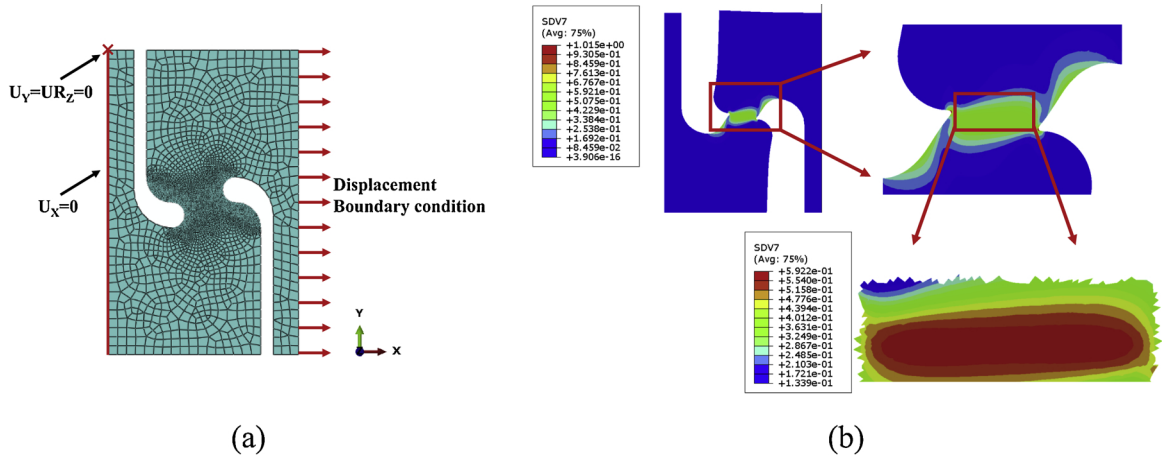

Fig. 15. Numerical model (a) and equivalent plastic strain field at the instant of failure (b) for a SH specimen deformed at 673 K and 0.001 s^{-1}.

available. The most convenient strategy to handle this problem is to use the constraint $r_b = 1$. Indeed, Banabic (2010) has shown that, for metallic sheets, this constraint can lead to well-shaped yield loci. As discussed earlier, the biaxial yield stress Y_b is not explicitly known. It can however be indirectly estimated from free bulging tests with an inverse method to fit the experimental dome height evolution. When the biaxial yield stress is known, one can obtain the following set of 8 equations (Banabic, 2005):

$$\begin{aligned}
&\bar{\sigma}(\boldsymbol{\sigma_0}, a, M, N, P, Q, R, S, T) - Y = 0\\
&\bar{\sigma}(\boldsymbol{\sigma_{45}}, a, M, N, P, Q, R, S, T) - Y = 0\\
&\bar{\sigma}(\boldsymbol{\sigma_{90}}, a, M, N, P, Q, R, S, T) - Y = 0\\
&\bar{\sigma}(\boldsymbol{\sigma_b}, a, M, N, P, Q, R, S, T) - Y = 0\\
&r_0(\boldsymbol{\sigma_0}, a, M, N, P, Q, R, S, T) - r_0^{\exp} = 0\\
&r_{45}(\boldsymbol{\sigma_{45}}, a, M, N, P, Q, R, S, T) - r_{45}^{\exp} = 0\\
&r_{90}(\boldsymbol{\sigma_{90}}, a, M, N, P, Q, R, S, T) - r_{90}^{\exp} = 0\\
&r_b(\boldsymbol{\sigma_b}, a, M, N, P, Q, R, S, T) - r_b^{\exp} = 0
\end{aligned} \tag{15}$$

where $\boldsymbol{\sigma_0}$, $\boldsymbol{\sigma_{45}}$ and $\boldsymbol{\sigma_{90}}$ are the stress tensors for uniaxial tension along the 0°, 45° and 90° directions, respectively. $\boldsymbol{\sigma_b}$ represents the stress tensor for biaxial tension. The detailed process leading to the above equation system can be found in the work of Banabic (2005). In the above equations, Y is selected as the uniaxial yield stress along the rolling direction at 673 K and 0.001 s^{-1}. For the resolution of this non-linear equation system, an improved Newton Raphson method, which refers to the work of Banabic (2010), is employed. The convergence of this algorithm depends on the initial vector choice. In the present study, this vector is fixed to [0.7, 1.2, 1, 1, 1, 1, 1, 1] which allows convergence.

As shown in Fig. 11, because the biaxial yield stress is unknown at the beginning of the identification procedure, an iterative procedure is used to determine the yield criterion parameters. This procedure uses the experimental data obtained from the free bulging tests with different constant pressures. Specifically, with some estimated yield criterion parameters, numerical simulations of the bulging tests with constant pressures (0.6 MPa, 1.0 MPa and 1.5 MPa) and constant temperature (673 K) are carried out. The numerical and experimental dome height evolutions are compared to each other, which allows adjusting the biaxial yield stress. The new biaxial yield stress is then used as an input of the Newton-Raphson algorithm to obtain a new estimation of the yield criterion parameters. This procedure is repeated until the dome height evolution is correctly reproduced.

The employed numerical model for free bulging test simulations is presented in Fig. 12. Only a quarter of the part is considered due to symmetry planes. The forming pressure is applied on the upper face of the sheet. The interaction between the sheet (slave) and the die (master) is controlled with a hard contact algorithm (surface to surface) with Coulomb friction of 0.1 (Nazzal et al., 2004). Shell elements with reduced integration are chosen for the sheet while both the die and blank holder are defined as discrete rigid surfaces.

The final BBC2003 yield criterion parameters are listed in Table 5. The corresponding biaxial yield stress at 673 K and 0.001 s^{-1} is Y_b = 35.3 MPa. The computed ratio between the biaxial yield stress and the uniaxial yield stress along the rolling direction at 673 K and 0.001 s^{-1} is around 1.32, which is significantly different from the unity value that one would obtain under the assumption of isotropy. As shown in Fig. 13, this estimation of the biaxial yield stress allows correctly reproducing the evolution of the dome height for the different forming pressures.

The predicted directional r-values and the uniaxial yield stresses in comparison to experimental data are shown in Fig. 14(a) and (b), respectively. It can be see that the solution obtained by the Newton-Raphson method meets the experimental values exactly. The yield locus predicted by this method also agrees with the experimental data very well (see Fig. 14(c)).

5.5. Fracture criterion parameters

5.5.1. Determination of equivalent fracture strains

The identification of the MMC criterion parameters relies on the equivalent plastic strains at fracture for different loading paths. These fracture strains have been determined using numerical simulation. Firstly, some simulations of SH, CH, NT20, NT10, NT5 and FB tests have been performed at 673 K and 0.001 s^{-1} to determine fracture strains for different stress states. Simulations of the NT20 test have then been conducted to obtain fracture strains under different deformation

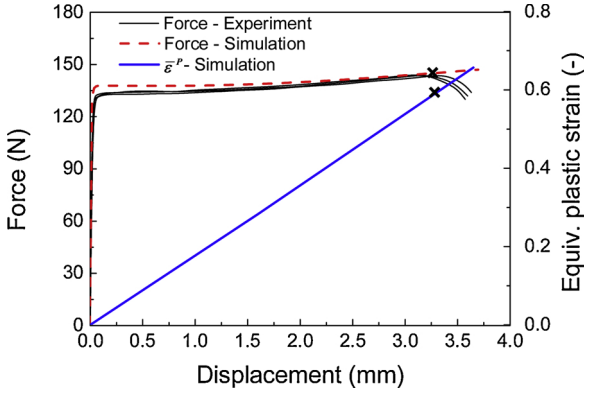

Fig. 16. Comparison of force-displacement curves between experimental and numerical results and equivalent plastic strain versus displacement for a SH specimen deformed at 673 K and 0.001 s^{-1}.

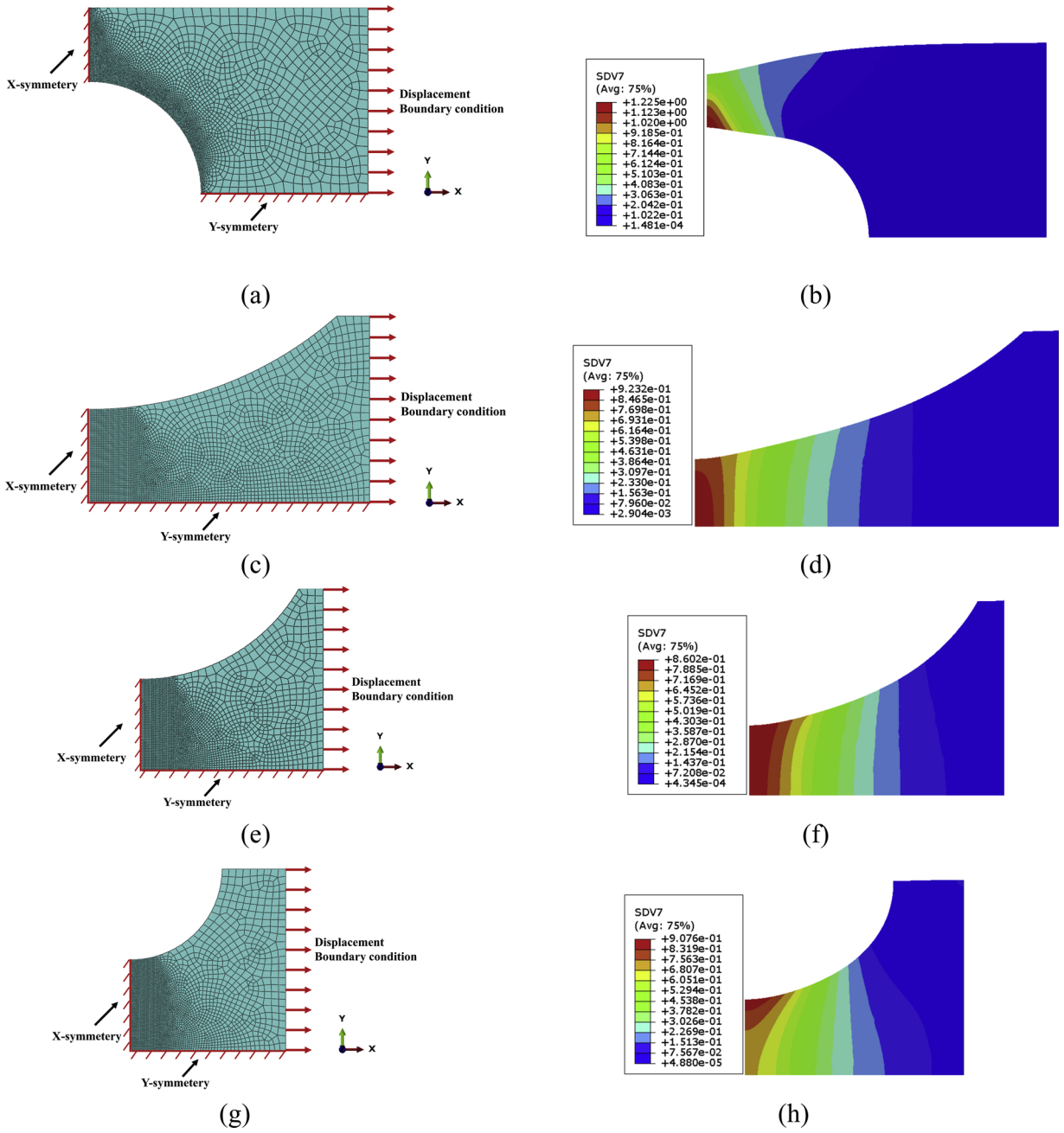

Fig. 17. Numerical models for CH test (a), NT20 test (c), NT10 test (e), NT5 test (f) and equivalent plastic strain fields at the instant of failure for a CH specimen (b), a NT20 specimen (d), a NT10 specimen (f) and a NT5 specimen (h) deformed at 673 K and 0.001 s^{-1}.

temperatures and strain rates. The displacement or force boundary conditions for the numerical simulations are identical to the corresponding experiments.

5.5.1.1. SH simulation at 673 K and 0.001 s^{-1}. Fig. 15(a) presents the numerical model for the SH test. The mesh size in the middle part is set to 0.1 mm to ensure convergence. Fig. 15(b) shows that the equivalent plastic strain field at fracture elongation is quite homogeneous in the middle part of the specimen. The average equivalent fracture strain has been calculated in this area. The calculated equivalent plastic strain evolution and force-displacement curves are illustrated by Fig. 16.

5.5.1.2. CH and NT simulations at 673 K and 0.001 s^{-1}. The numerical models for central hole tension and notched tension tests are shown in Fig. 17(a, c, e, g). The element size has been set to 0.1, 0.2, 0.15 and 0.1 mm in the central region of CH, NT20, NT10 and NT5 specimens, respectively. Fig. 17*(b, d, f, h) present the equivalent plastic strain field at the instant of fracture for different specimen geometries. The maximum equivalent plastic strain is found at the hole surface for CH specimens. For NT20 and NT10 specimens, the maximum equivalent plastic strain is localized in the center of the specimen.* The maximum equivalent plastic strain for NT5 specimen is found around the notch edges, which is in agreement with experimental observations of fractured specimens.

The experimental and numerical force-displacement curves at 673 K and 0.001 s^{-1} together with the corresponding equivalent plastic strain evolutions for the central hole and notched specimens are shown in Fig. 18. The agreement between experimental and numerical data is generally good, which indicates that the employed constitutive model is capable of considering the impact of the stress state on the deformation behavior.

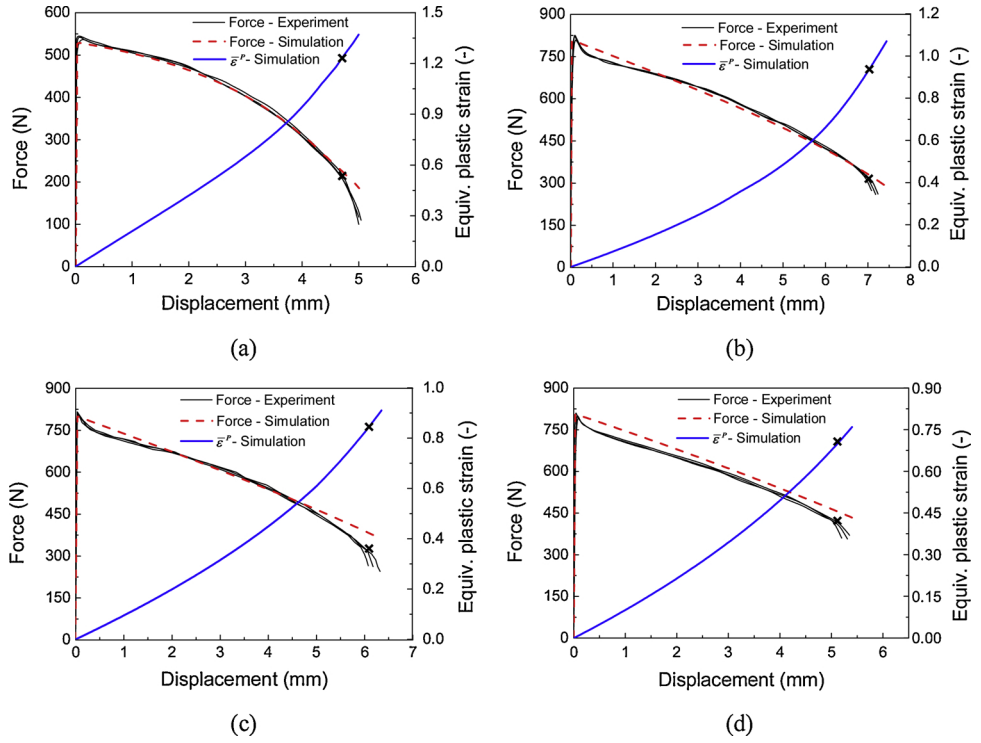

Fig. 18. Comparison of force-displacement curves between experimental and numerical results and equivalent plastic strain versus displacement for a CH specimen (a), a NT20 specimen (b), a NT10 specimen (c) and a NT5 specimen (d) deformed at 673 K and 0.001 s^{-1}.

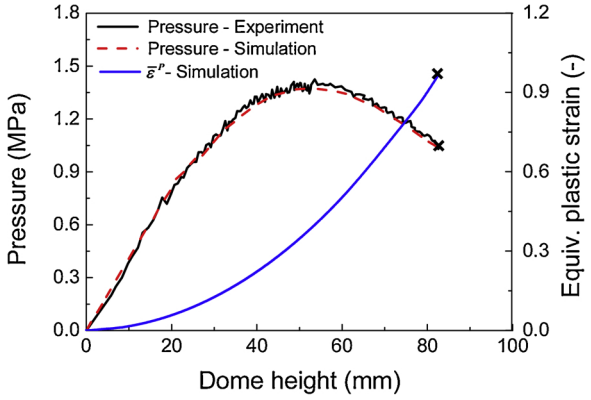

Fig. 19. Comparison of force-displacement curves between experimental and numerical results and equivalent plastic strain versus displacement for a FB specimen deformed at 673 K and 0.001 s^{-1}.

5.5.1.3. FB simulation at 673 K and 0.001 s^{-1}. The numerical model for the FB test at constant strain rate is similar to the one used for simulations at constant forming pressures (see Fig. 12). Mesh convergence is achieved with a mesh size of 1.0 mm. The experimental and calculated pressure versus displacement curves are in a good agreement (Fig. 19). The evolution of the equivalent plastic strain at the dome apex, which is the fracture initiation position, is also plotted.

5.5.1.4. NT20 simulations at different temperatures and strain rates. In our study, NT20 tests have been used to investigate the temperature and strain rate effect on the ductile fracture behavior. The corresponding simulations have been performed to estimate the equivalent fracture strains in the studied temperature and strain rate range. The numerical model has been presented in Fig. 17. The comparison between the experimental and numerical force versus displacement curves is displayed in Fig. 20. When the displacement exceeds 1 mm, the agreement between numerical and experimental is correct. However, at the onset of plastic deformation, especially for high strain rates, the sudden reduction of axial force is not reproduced by the numerical model. This aspect is due to the fact the yield drop phenomenon has not been taken into consideration in the constitutive model.

5.5.2. Determination of fracture criterion parameters

The fracture strains obtained from the different simulations are listed in Table 6. According to the results, the equivalent fracture strain strongly depends on the strain rate, temperature and stress state. Generally speaking, during a deformation process, the stress state is variable so that the triaxiality is not constant. To determine the fracture locus, the method suggested by Bao and Wierzbicki (2004) is used. It consists in determining the average value of the stress triaxiality. For a given loading path, the average triaxiality value η_{av} is obtained from:

$$\eta_{av} = \frac{1}{\bar{\varepsilon}_f^P} \int_0^{\bar{\varepsilon}_f^P} \eta(\bar{\varepsilon}^P) d\bar{\varepsilon}^P \tag{16}$$

where $\eta(\bar{\varepsilon}^P)$ is the stress triaxiality evolution from the numerical simulation. The evolution of the triaxiality $\eta(\bar{\varepsilon}^P)$ at 673 K and 0.001 s^{-1} is shown for all tested specimen geometries in Fig. 21. Except from the free bulging test, the stress triaxiality changes with the evolution of the equivalent plastic strain.

The MMC criterion employed in this work contains five original parameters (A, n', c_1, c_2, c_3) and three additional parameters (D_1, D_2, Z) to include the influence of strain rate, temperature and cut-off value. The reference strain rate is selected as $\dot{\bar{\varepsilon}}_{ref} = 0.001\ s^{-1}$ while the reference temperature as $T_{ref} = 623$ K. The criterion parameters have been calibrated by minimizing the objective function $\Re_D$:

$$\Re_D(A, c_1, c_2, c_3, n', D_1, D_2, Z) = \sqrt{\frac{1}{N}\sum_{i=1}^{N} (\exp \bar{\varepsilon}_{f,i}^P - ^{pre}\ \bar{\varepsilon}_{f,i}^P(\eta, \dot{\bar{\varepsilon}}^P, \theta))^2} \tag{17}$$

where N is the number of calibration experiments. To identify the

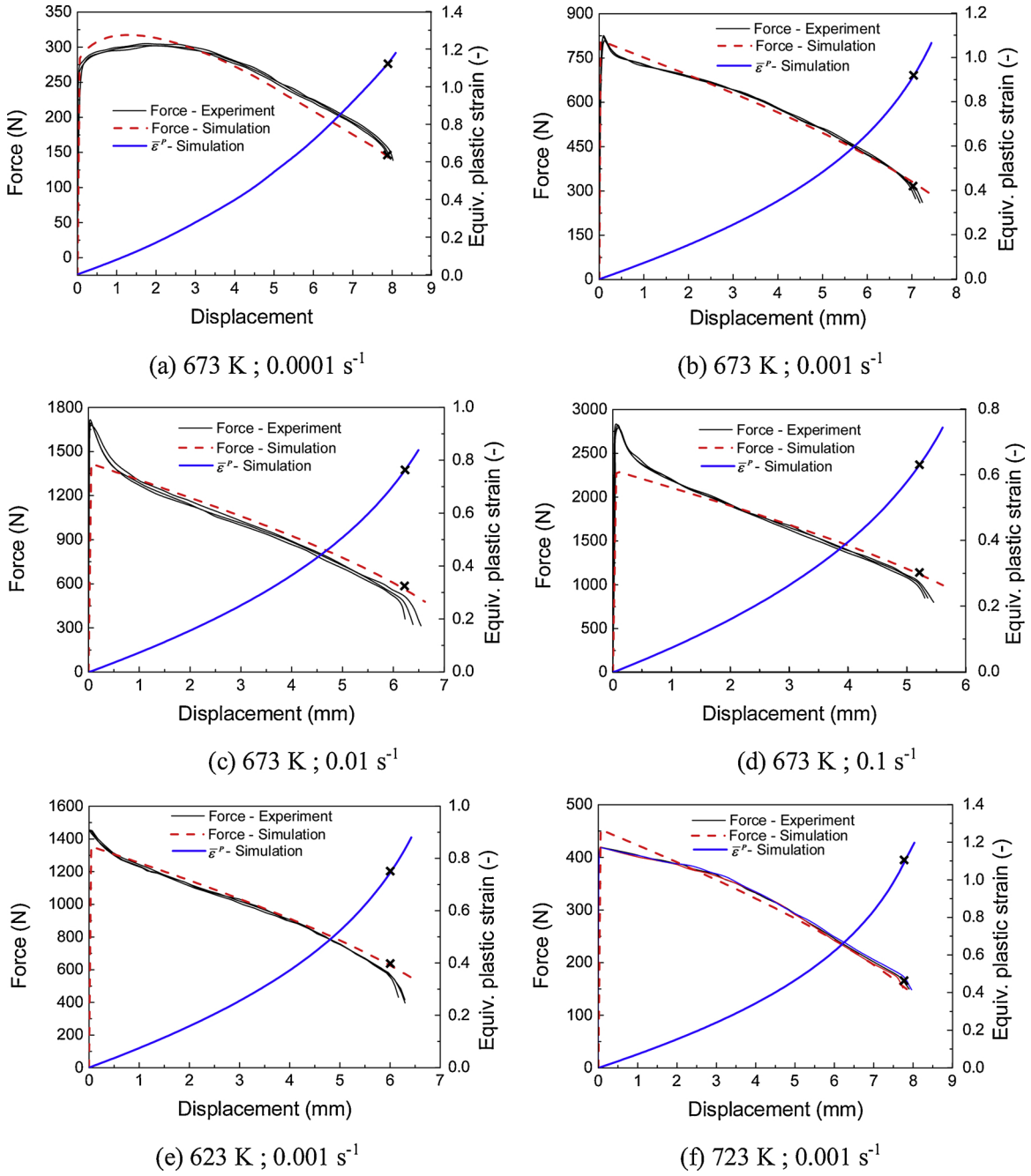

Fig. 20. Comparison of force-displacement curves between experimental and numerical results and equivalent plastic strain versus displacement for a NT20 specimen deformed at different temperatures and strain rates.

Table 6
Summary of the equivalent fracture strains for different specimen geometries and deformation temperatures and strain rates.

Geometry Conditions	SH	CH	NT20	NT10	NT5	FB
673 K ; 0.0001 s^{-1}			1.1			
673 K ; 0.001 s^{-1}	0.59	1.23	0.92	0.84	0.71	0.96
673 K ; 0.01 s^{-1}			0.76			
673 K ; 0.1 s^{-1}			0.63			
623 K ; 0.001 s^{-1}			0.75			
723 K ; 0.001 s^{-1}			1.1			

parameters, a genetic algorithm with 10 000 individuals, a mutation probability of 0.02 and a crossover probability of 0.8 has been used. The parameters of the MMC criterion for the AA5383 alloy are listed in Table 7.

The evolution of the fracture strain with respect to triaxiality at 673 K and 0.001 s^{-1} is shown in Fig. 22(a). The predictions of the fracture criterion are consistent with experimental trends. The fracture locus is divided into three domains according to the value of triaxiality: 0 ~ 0.33, 0.33 ~ 0.6 and 0.6 ~ 0.67. In the middle range, the equivalent fracture strain decreases with the triaxiality while opposite trends are observed for the other two ranges.

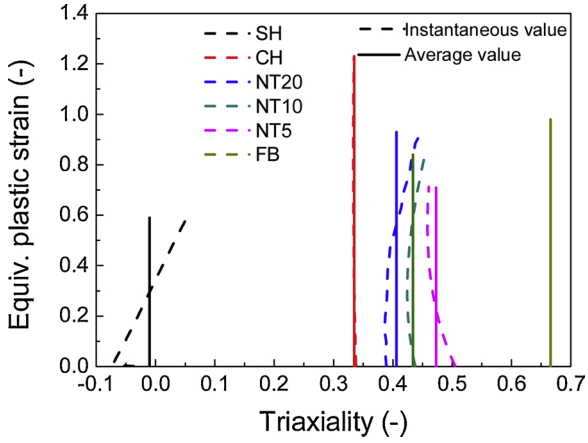

Fig. 21. Evolution of the stress triaxiality and the corresponding average values for different shape of specimen deformed at 673 K and 0.001 s^{-1}.

Table 7
Identified parameter values of MMC criterion and the corresponding residual value.

A [MPa]	c_1[-]	c_2[MPa]	c_3[-]	n'[-]	D_1 [-]	D_2 [-]	Z [-]	$\Re_D$[-]
157	−0.0036	75.27	0.960	0.135	−0.069	1.106	0.02	0.057

The response of the criterion when varying the temperature and the strain rate is illustrated by Fig. 22(b, c). The calibrated model gives a correct description of the impact of temperature and strain rate on the equivalent fracture strains.

6. Conclusions

In this study, the high temperature behavior of the AA5383 alloy has been investigated. For this purpose, different uniaxial and biaxial tests have been performed to characterize the plastic deformation behavior for different strain rates (10^{-4}∼10^{-1} s^{-1}) and temperatures (623∼723 K). Also, the impact of temperature, strain rate and triaxiality on ductile fracture has been evaluated with central hole tension, notched tension, shear and free bulging tests. To describe the deformation behavior of the AA5383 alloy, a viscoplastic flow rule, which includes the impact of temperature and strain hardening, has been proposed. The BBC2003 yield criterion is used to consider the significant anisotropic plastic deformation behavior. The prediction of ductile fracture uses the MMC uncoupled criterion of Bai and Wierzbicki (2010), which has been extended to include the impact of temperature and strain rate. The constitutive model has then been implemented within a finite element solver. Numerical simulations of the different experimental tests have been carried out to identify the flow rule, yield criterion and fracture criterion parameters. Except from the yield drop phenomenon, which is not accounted for, the numerical and experimental results of the different tests are in good agreement. In the future, the proposed model will be used to optimize process conditions for gas forming operations of complex-shaped parts.

CRediT authorship contribution statement

Rou Du: Conceptualization, Methodology, Software, Formal analysis, Investigation, Resources, Data curation, Writing - original draft, Visualization. **Charles Mareau:** Validation, Writing - review & editing, Supervision. **Yessine Ayed:** Supervision. **Eliane Giraud:** Supervision. **Philippe Dal Santo:** Supervision, Project administration, Funding acquisition.

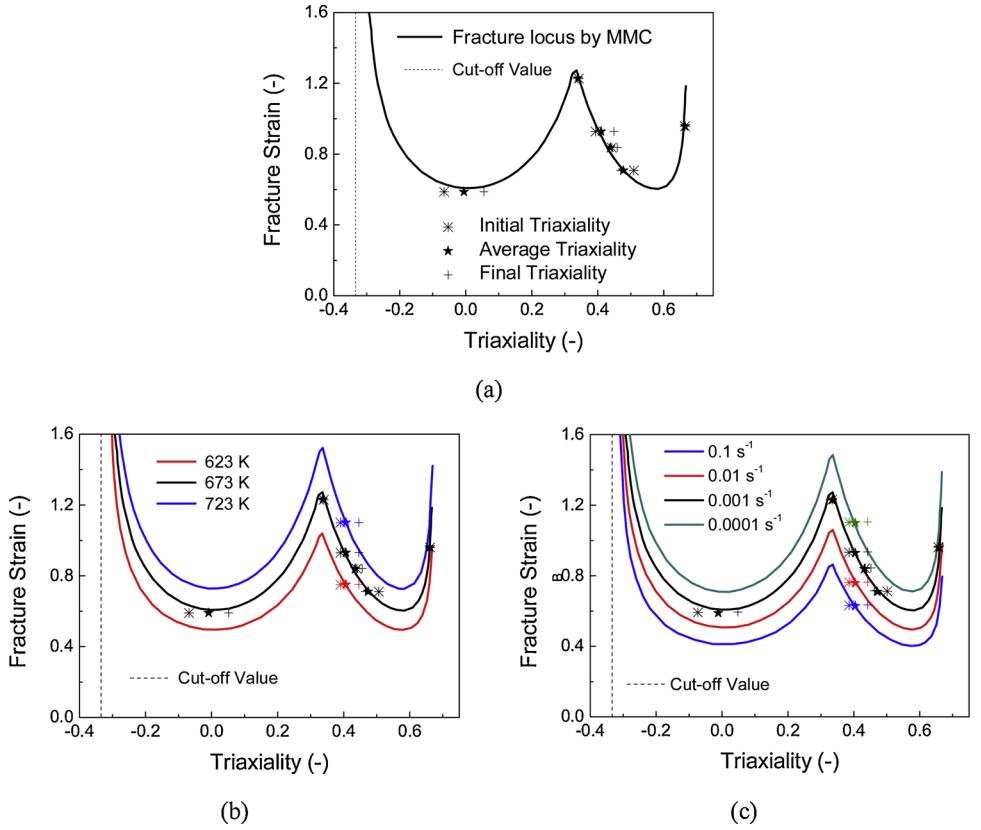

Fig. 22. Comparison between the fracture locus against stress triaxiality obtained from MMC criterion and the experimental data at 673 K and 0.001 s^{-1} (a), different temperatures (b) and different strain rates (c).

Declaration of Competing Interest

The authors declare that there are no conflicts of interest.

Acknowledgement

This work was financially supported by the China Scholarship council [File no. 201506020084]

Appendix A

Numerical implementation

The proposed constitutive model has been implemented within the implicit finite element solver ABAQUS/Standard with a user subroutine. This subroutine must return (i) the stress increment $\Delta\boldsymbol{\sigma}$ caused by a strain increment $\Delta\boldsymbol{\varepsilon}$ and a temperature increment $\Delta\theta$ and (ii) the tangent moduli tensor $\boldsymbol{L} = \partial\Delta\boldsymbol{\sigma}/\partial\Delta\boldsymbol{\varepsilon}$. For an elasto-viscoplastic constitutive model, the stress increment is connected to the strain increment with:

$$\Delta\boldsymbol{\sigma} = \boldsymbol{C}\colon(\Delta\boldsymbol{\varepsilon} - \Delta\boldsymbol{\varepsilon^p}) \tag{18}$$

where $\Delta\boldsymbol{\varepsilon^p}$ is the plastic strain tensor increment. Under the plane stress assumption, the Voigt representation of the elastic stiffness tensor $\boldsymbol{C}$ from the Young's modulus E and Poisson's ratio ν is:

$$\boldsymbol{C} = \frac{E}{1-\nu^2}\begin{vmatrix} 1 & \nu & 0 \\ \nu & 1 & 0 \\ 0 & 0 & 1-\nu \end{vmatrix} \tag{19}$$

The plastic strain tensor increment $\Delta\boldsymbol{\varepsilon^p}$ is given by:

$$\Delta\boldsymbol{\varepsilon^p} = \Delta\bar{\varepsilon}^p\boldsymbol{n} \tag{20}$$

where $\Delta\bar{\varepsilon}^p$ is the equivalent plastic strain increment and $\boldsymbol{n}$ is the plastic flow direction, which is assumed to be constant during an integration step. According to the normality rule, the flow direction is obtained from:

$$\boldsymbol{n} = \left.\frac{\partial\Phi}{\partial\boldsymbol{\sigma}}\right|_t \tag{21}$$

To estimate the equivalent plastic strain increment, a semi-implicit method is used. This method consists in expressing the equivalent plastic strain increment as follows:

$$\Delta\bar{\varepsilon}^p = (1-\alpha)\dot{\bar{\varepsilon}}_t^p\Delta t + \alpha\dot{\bar{\varepsilon}}_{t+\Delta t}^p\Delta t \tag{22}$$

where Δt is the time increment and α is a numerical parameter that allows controlling the explicit/implicit character of the numerical integration scheme. The initial and final equivalent plastic strain rates are respectively denoted by $\dot{\bar{\varepsilon}}_t^p$ and $\dot{\bar{\varepsilon}}_{t+\Delta t}^p$. According to the proposed constitutive model, the initial equivalent plastic strain rate is given by:

$$\dot{\bar{\varepsilon}}_t^p = \left(\frac{\bar{\sigma}_t}{K(\bar{\varepsilon}_t^p + \bar{\varepsilon}_0^p)^n \exp(-b\bar{\varepsilon}_t^p)\left(1 - \left(\frac{\theta_t - \theta_{ref}}{\theta_m - \theta_{ref}}\right)^\beta\right)}\right)^{1/m} \tag{23}$$

where $\bar{\sigma}_t$, $\bar{\varepsilon}_t^p$ and θ_t are respectively the initial equivalent stress, equivalent plastic strain and temperature. The final equivalent plastic strain rate is obtained from a first order Taylor expansion, that is:

$$\dot{\bar{\varepsilon}}_{t+\Delta t}^p = \dot{\bar{\varepsilon}}_t^p + \left.\frac{\partial\dot{\bar{\varepsilon}}^p}{\partial\bar{\sigma}}\right|_t\Delta\bar{\sigma} + \left.\frac{\partial\dot{\bar{\varepsilon}}^p}{\partial\theta}\right|_t\Delta\theta + \left.\frac{\partial\dot{\bar{\varepsilon}}^p}{\partial\bar{\varepsilon}^p}\right|_t\Delta\bar{\varepsilon}^p \tag{24}$$

While the derivatives of the equivalent plastic strain rate with respect to the equivalent stress, the temperature and the equivalent plastic strain are easily obtained from the viscoplastic flow rule, the equivalent stress increment is given by:

$$\begin{aligned}\Delta\bar{\sigma} &= \boldsymbol{n}\colon\Delta\boldsymbol{\sigma} \\ &= \boldsymbol{n}\colon\boldsymbol{C}\colon(\Delta\boldsymbol{\varepsilon} - \Delta\boldsymbol{\varepsilon^p}) \\ &= \boldsymbol{n}\colon\boldsymbol{C}\colon(\Delta\boldsymbol{\varepsilon} - \boldsymbol{n}\Delta\bar{\varepsilon}^p)\end{aligned} \tag{25}$$

Combining the above relations leads to the following linear equation for the equivalent plastic strain increment

$$\Delta\bar{\varepsilon}^p = \dot{\bar{\varepsilon}}_t^p\Delta t + \alpha\Delta t\left(\left.\frac{\partial\dot{\bar{\varepsilon}}^p}{\partial\bar{\sigma}}\right|_t\boldsymbol{n}\colon\boldsymbol{C}\colon(\Delta\boldsymbol{\varepsilon} - \boldsymbol{n}\Delta\bar{\varepsilon}^p) + \left.\frac{\partial\dot{\bar{\varepsilon}}^p}{\partial\theta}\right|_t\Delta\theta + \left.\frac{\partial\dot{\bar{\varepsilon}}^p}{\partial\bar{\varepsilon}^p}\right|_t\Delta\bar{\varepsilon}^p\right) \tag{26}$$

The plastic strain increment is therefore estimated from

$$\Delta\bar{\varepsilon}^p = \frac{\dot{\bar{\varepsilon}}_t^p\Delta t + \alpha\Delta t\left(\left.\frac{\partial\dot{\bar{\varepsilon}}^p}{\partial\bar{\sigma}}\right|_t\boldsymbol{n}\colon\boldsymbol{C}\colon\Delta\boldsymbol{\varepsilon} + \left.\frac{\partial\dot{\bar{\varepsilon}}^p}{\partial\theta}\right|_t\Delta\theta\right)}{1 + \alpha\Delta t\left(\left.\frac{\partial\dot{\bar{\varepsilon}}^p}{\partial\bar{\sigma}}\right|_t\boldsymbol{n}\colon\boldsymbol{C}\colon\boldsymbol{n} - \left.\frac{\partial\dot{\bar{\varepsilon}}^p}{\partial\bar{\varepsilon}^p}\right|_t\right)} \tag{27}$$

Using the above estimation of the plastic strain increment, the tangent moduli tensor is calculated from

$$\boldsymbol{L} = \boldsymbol{C}\colon\left(\boldsymbol{I} - \boldsymbol{n}\otimes\frac{\partial\Delta\bar{\varepsilon}^{p}}{\partial\Delta\boldsymbol{\varepsilon}}\right) \tag{28}$$

with

$$\frac{\partial\Delta\bar{\varepsilon}^{p}}{\partial\Delta\boldsymbol{\varepsilon}} = \frac{\alpha\Delta t\left.\frac{\partial\dot{\bar{\varepsilon}}^{p}}{\partial\bar{\sigma}}\right|_{t}\boldsymbol{n}\colon\boldsymbol{C}\colon\Delta\boldsymbol{\varepsilon}}{1+\alpha\Delta t\left(\left.\frac{\partial\dot{\bar{\varepsilon}}^{p}}{\partial\bar{\sigma}}\right|_{t}\boldsymbol{n}\colon\boldsymbol{C}\colon\boldsymbol{n}-\left.\frac{\partial\dot{\bar{\varepsilon}}^{p}}{\partial\bar{\varepsilon}^{p}}\right|_{t}\right)} \tag{29}$$

References

Agarwal, S., Krajewski, P., Briant, C., 2008. Dynamic recrystallization of AA5083 at 450° C: the effects of strain rate and particle size. Metall. Mater. Trans. A 39, 1277–1289. https://doi.org/10.1007/s11661-008-9476-7.

Aksenov, S.A., Kolesnikov, A.V., Mikhaylovskaya, A.V., 2016. Design of a gas forming technology using the material constants obtained by tensile and free bulging testing. J. Mater. Process. Technol. 237, 88–95. https://doi.org/10.1016/j.jmatprotec.2016.06.003.

Bai, Y., Wierzbicki, T., 2008. A new model of metal plasticity and fracture with pressure and Lode dependence. Int. J. Plast. 24, 1071–1096. https://doi.org/10.1016/j.ijplas.2007.09.004.

Bai, Y., Wierzbicki, T., 2010. Application of extended Mohr–Coulomb criterion to ductile fracture. Int. J. Fract. Mech. 161, 1. https://doi.org/10.1007/s10704-009-9422-8.

Banabic, D., 2005. An improved analytical description of orthotropy in metallic sheets. Int. J. Plast. 21, 493–512. https://doi.org/10.1016/j.ijplas.2004.04.003.

Banabic, D., 2010. Plastic Behaviour of Sheet Metal, Sheet Metal Forming Processes. Springer, pp. 27–140. https://doi.org/10.1007/978-3-540-88113-1_2.

Bao, Y., Wierzbicki, T., 2004. On fracture locus in the equivalent strain and stress triaxiality space. Int. J. Mech. Sci. 46, 81–98. https://doi.org/10.1016/j.ijmecsci.2004.02.006.

Bao, Y., Wierzbicki, T., 2005. On the cut-off value of negative triaxiality for fracture. Eng. Fract. Mech. 72, 1049–1069. https://doi.org/10.1016/j.engfracmech.2004.07.011.

Chen, G., Ren, C., Yu, W., Yang, X., Zhang, L., 2012. Application of genetic algorithms for optimizing the Johnson–Cook constitutive model parameters when simulating the titanium alloy Ti-6Al-4V machining process. Proc. Inst. Mech. Eng. Pt. B: J. Eng. Manuf. 226, 1287–1297. https://doi.org/10.1177/0954405412447735.

Cockcroft, M., Latham, D., 1968. Ductility and the workability of metals. J. Inst. Metals 96, 33–39. https://doi.org/10.1080/14735786809366362.

Driver, J., Engler, O., 2004. Design of aluminum rolling processes for foil, sheet, and plate. Mater. Eng. (New York) 24, 69–114. https://doi.org/10.1201/9780203970928.ch4.

Gao, X., Zhang, T., Zhou, J., Graham, S.M., Hayden, M., Roe, C., 2011. On stress-state dependent plasticity modeling: significance of the hydrostatic stress, the third invariant of stress deviator and the non-associated flow rule. Int. J. Plast. 27, 217–231. https://doi.org/10.1016/j.ijplas.2010.05.004.

Grujicic, M., Pandurangan, B., Yen, C.F., Cheeseman, B.A., 2011. Modifications in the AA5083 Johnson-Cook material model for use in friction stir welding computational analyses. J. Mater. Eng. Perform. 21, 2207–2217. https://doi.org/10.1007/s11665-011-0118-7.

Hu, Q., Li, X., Han, X., Chen, J., 2017. A new shear and tension based ductile fracture criterion: modeling and validation. Eur. J. Mech. A-Solid. 66, 370–386. https://doi.org/10.1016/j.euromechsol.2017.08.005.

Jarrar, F.S., Hector, L.G., Khraisheh, M.K., Bower, A.F., 2010. New approach to gas pressure profile prediction for high temperature AA5083 sheet forming. J. Mater. Process. Technol. 210, 825–834. https://doi.org/10.1016/j.jmatprotec.2010.01.002.

Johnson, G.R., Cook, W.H., 1983. A constitutive model and data for materials subjected to large strains, high strain rates, and high temperatures. In: Proc. 7th Inf. Sympo. Ballistics. pp. 541–547.

Johnson, G.R., Cook, W.H., 1985. Fracture characteristics of three metals subjected to various strains, strain rates, temperatures and pressures. Eng. Fract. Mech. 21, 31–48. https://doi.org/10.1016/0013-7944(85)90052-9.

Kaibyshev, R., Musin, F., Avtokratova, E., Motohashi, Y., 2005. Deformation behavior of a modified 5083 aluminum alloy. Mater. Sci. Eng. A 392, 373–379. https://doi.org/10.1016/j.msea.2004.10.002.

Kocks, W.F., 1975. Thermodynamics and kinetics of slip. Progr. Mater. Sci. 19, 291.

Li, Y., Luo, M., Gerlach, J., Wierzbicki, T., 2010. Prediction of shear-induced fracture in sheet metal forming. J. Mater. Process. Technol. 210, 1858–1869. https://doi.org/10.1016/j.jmatprotec.2010.06.021.

Li, H., Fu, M., Lu, J., Yang, H., 2011. Ductile fracture: experiments and computations. Int. J. Plast. 27, 147–180. https://doi.org/10.1016/j.ijplas.2010.04.001.

Liu, J., Tan, M.-J., Jarfors, A.-E.-W., Aue-u-lan, Y., Castagne, S., 2010. Formability in AA5083 and AA6061 alloys for light weight applications. Mater. Des. 31, S66–S70. https://doi.org/10.1016/j.matdes.2009.10.052.

Lou, Y., Huh, H., Lim, S., Pack, K., 2012. New ductile fracture criterion for prediction of fracture forming limit diagrams of sheet metals. Int. J. Solids Struct. 49, 3605–3615. https://doi.org/10.1016/j.ijsolstr.2012.02.016.

Lou, Y., Yoon, J.W., Huh, H., 2014. Modeling of shear ductile fracture considering a changeable cut-off value for stress triaxiality. Int. J. Plast. 54, 56–80. https://doi.org/10.1016/j.ijplas.2013.08.006.

Magee, A.C., Ladani, L., 2013. Temperature dependency of mechanical behavior and strain rate sensitivity of an Al–Mg alloy with bimodal grain size. Mater. Sci. Eng. A 582, 276–283. https://doi.org/10.1016/j.msea.2013.06.016.

Majzoobi, G.H., Kashfi, M., Bonora, N., Iannitti, G., Ruggiero, A., Khademi, E., 2018. Damage characterization of aluminum 2024 thin sheet for different stress triaxialities. Arch. Civ. Mech. Eng. 18, 702–712. https://doi.org/10.1016/j.acme.2017.11.003.

Mohr, D., Marcadet, S.J., 2015. Micromechanically-motivated phenomenological Hosford–Coulomb model for predicting ductile fracture initiation at low stress triaxialities. Int. J. Solids Struct. 67-68, 40–55. https://doi.org/10.1016/j.ijsolstr.2015.02.024.

Naka, T., Torikai, G., Hino, R., Yoshida, F., 2001. The effects of temperature and forming speed on the forming limit diagram for type 5083 aluminum–magnesium alloy sheet. J. Mater. Process. Technol. 113, 648–653. https://doi.org/10.1016/s0924-0136(01)00650-1.

Naka, T., Nakayama, Y., Uemori, T., Hino, R., Yoshida, F., 2003. Effects of temperature on yield locus for 5083 aluminum alloy sheet. J. Mater. Process. Technol. 140, 494–499. https://doi.org/10.1016/s0924-0136(03)00780-5.

Nazzal, M.A., Khraisheh, M.K., Darras, B.M., 2004. Finite element modeling and optimization of superplastic forming using variable strain rate approach. J. Mater. Eng. Perform. 13, 691–699. https://doi.org/10.1361/10599490421321.

Oyane, M., 1972. Criteria of ductile fracture strain. Bull. Jsme 15, 1507–1513. https://doi.org/10.1299/jsme1958.15.1507.

Peirs, J., Verleysen, P., Degrieck, J., 2012. Novel technique for static and dynamic shear testing of Ti6Al4V sheet. Exp. Mech. 52, 729–741. https://doi.org/10.1007/s11340-011-9541-9.

Qian, L.-Y., Fang, G., Zeng, P., 2017. Modeling of the ductile fracture during the sheet forming of aluminum alloy considering non-associated constitutive characteristic. Int. J. Mech. Sci. 126, 55–66. https://doi.org/10.1016/j.ijmecsci.2017.03.013.

Raynaud, G., Gomiero, P., 1997. The potential of 5383 alloy in marine applications. The Aluminum Association (USA) 351–364.

Skippon, T., Mareau, C., Daymond, M., 2012. On the determination of single-crystal plasticity parameters by diffraction: optimization of a polycrystalline plasticity model using a genetic algorithm. J. Appl. Crystallogr. 45, 627–643. https://doi.org/10.1107/S0021889812026854.

Summers, P.T., Chen, Y., Rippe, C.M., Allen, B., Mouritz, A.P., Case, S.W., Lattimer, B.Y., 2015. Overview of aluminum alloy mechanical properties during and after fires. Fire Sci. Rev. 4, 3. https://doi.org/10.1186/s40038-015-0007-5.

Sung, J.H., Kim, J.H., Wagoner, R.H., 2010. A plastic constitutive equation incorporating strain, strain-rate, and temperature. Int. J. Plast. 26, 1746–1771. https://doi.org/10.1016/j.ijplas.2010.02.005.

Teng, B., Wang, W., Xu, Y., 2017. Ductile fracture prediction in aluminium alloy 5A06 sheet forming based on GTN damage model. Eng. Fract. Mech. 186, 242–254. https://doi.org/10.1016/j.engfracmech.2017.10.014.

Voyiadjis, G.Z., Abed, F.H., 2005. Microstructural based models for bcc and fcc metals with temperature and strain rate dependency. Mech. Mater. 37, 355–378. https://doi.org/10.1016/j.mechmat.2004.02.003.